Realizable versus non-realizable dynamic subgrid-scale stress models

Stefan Heinz[a)] and Harish Gopalan

Department of Mathematics, University of Wyoming, 1000 East University Avenue, Laramie, Wyoming 82071, USA

The existence of many different dynamic large eddy simulation (LES) methods leads to questions about the theoretical foundation of dynamic LES methods. It was shown recently that the use of stochastic analysis enables a theoretically well based systematic derivation of a realizable linear dynamic model (LDM) and a realizable nonlinear dynamic model (NDM). *A priori* and *a posteriori* analyses of turbulent channel flow are used here to study the characteristic properties of these dynamic models. The LDM and NDM are compared with other dynamic models: the non-stabilized and stabilized dynamic Smagorinsky model (DSM), which is used in many applications of LES, and Wang-Bergstrom's dynamic model (WBDM), which represents an extension of the DSM. The DSM and WBDM do not represent realizable models because they are not derived as consequences of a realizable stochastic process. The comparisons reported here show that the LDM and NDM are based on a dynamic model formulation that avoids shortcomings of existing concepts. The LDM and NDM account for backscatter, and they are computationally stable without any modification. The LDM and NDM represent the instantaneous small scale structure of turbulence very well. Compared to the DSM and WBDM, respectively, the LDM and NDM are computationally more efficient. © *2012 American Institute of Physics.* [http://dx.doi.org/10.1063/1.4767538]

I. INTRODUCTION

Large eddy simulation (LES) represents a very promising method to address many relevant engineering and environmental problems.[1–8] The price for reducing the computational cost of direct numerical simulation (DNS) by the consideration of LES equations is a closure problem given by the appearance of the unknown deviatoric subgrid-scale (SGS) stress tensor τ_{ij}^d in LES equations. The simple Smagorinsky model $\tau_{ij}^d = -2\nu_t \widetilde{S}_{ij}$ is often used as a model for the deviatoric SGS stress,[9] where incompressible flow is considered for simplicity. Here, $\widetilde{S}_{ij}$ refers to the filtered rate-of-strain tensor and $\nu_t = C_s \Delta^2 |\tilde{S}|$ is the SGS viscosity. This viscosity involves the Smagorinsky constant C_s, the filter width Δ, and the filtered characteristic strain rate $|\widetilde{S}| = (2\widetilde{S}_{ij} \, \widetilde{S}_{ji})^{1/2}$. The sum convention is used throughout this paper. The calculation of the SGS stress using the Smagorinsky model requires the specification of the model parameter C_s. The simplest choice is a constant positive C_s value. However, there are two main problems associated with the use of a constant C_s. First, a constant C_s turned out to be inappropriate to accurately calculate, for example, laminar flows, transitional flows and near-wall regions.[5–8] Second, the Smagorinsky model cannot account for backscatter of energy from the small scales to large scales, which requires negative C_s values.

A solution for this problem was pioneered by Germano who introduced the idea of dynamic SGS stress models.[10–12] The dynamic Smagorinsky model (DSM) is based on Germano's identity $L_{ij}^d = T_{ij}^d - \overline{\tau_{ij}^d}$. Here, L_{ij}^d is the known deviatoric Leonard stress, T_{ij}^d is the unknown deviatoric

---

a)Electronic mail: heinz@uwyo.edu.

    24, 115105-1

subtest-scale (STS) stress, and $\overline{\tau_{ij}^d}$ is the known deviatoric test-filtered SGS stress. In correspondence to the Smagorinsky model, Germano *et al.*[10] assumed the expression $T_{ij}^d = -2\nu_t^T \widetilde{\overline{S}}_{ij}$ for the deviatoric STS stress. Here, $\widetilde{\overline{S}}_{ij}$ is the test-scale strain tensor and $\nu_t^T = C_s(\Delta^T)^2 |\widetilde{\overline{S}}|$ refers to the STS viscosity, where Δ^T and $|\widetilde{\overline{S}}| = (2\widetilde{\overline{S}}_{kl}\widetilde{\overline{S}}_{lk})^{1/2}$ are the test filter width and test-scale characteristic strain rate, respectively. By using this expression for T_{ij}^d in Germano's identity one obtains an equation which can be used to compute local C_s values (see Appendix A). However, numerical simulations performed using the DSM lead to the appearance of large negative values of C_s, which implies computational instability. A possible explanation for this instability is the following:[13,14] This instability can be traced to the fact that C_s has a large auto-correlation time. Therefore, once it becomes negative in some region, it may remain negative for excessively long periods of time during which the exponential growth of the local velocity fields, associated with a negative eddy viscosity, causes a divergence of the total energy.

One way to overcome the DSM instability problem (a global stabilization) is to stabilize the model by averaging C_s over directions of statistical homogeneity and using clipping procedures for negative C_s values. Unfortunately, this stabilized dynamic Smagorinsky model it is not applicable to complex-geometry inhomogeneous flows. A solution for this problem was suggested by Meneveau *et al.*[12] The resulting Lagrangian dynamic model is applicable to inhomogeneous flows in complex geometries. The SGS stress implied by both, the stabilized dynamic Smagorinsky and Lagrangian dynamic model, has desirable features: it vanishes in laminar flow, and it has the correct asymptotic behavior near a solid boundary. A second way to overcome the DSM instability problem (a local stabilization) is to assume a balance equation for C_s. This can be done, for example, by using an integral equation for C_s, which does not use the assumption that C_s is unaffected by the test filtering of the SGS stress,[14] or by using a nonlinear SGS stress model that contains more than one dynamic constant:[15] see Appendix B. Other ways to address the DSM instability problem are described, for example, in Refs. 7 and 16–22.

The variety of available dynamic LES models leads to the question of which model should be preferred. A dynamic method can be considered to represent an optimal method if it has the following properties:

P1:   It is not an *ad hoc* procedure but implied by proven turbulence properties.[14]
P2:   It provides local model parameters, which is relevant to transitional flow simulations.[23]
P3:   It allows negative model parameters to enable the simulation of backscatter.[16]
P4:   It enables computationally stable simulations without additional *ad hoc* assumptions.
P5:   No other dynamic method applied to the same stress structure performs better in simulations (is either faster or more accurate).

Most previously developed dynamic models combine Germano's identity with a SGS and STS stress that have the same structure (like $\tau_{ij}^d = -2C_s\Delta^2|\tilde{S}|\tilde{S}_{ij}$ and $T_{ij}^d = -2C_s(\Delta^T)^2|\widetilde{\overline{S}}|\widetilde{\overline{S}}_{ij}$, see above). However, this equal-structure assumption applied to the STS stress is only an assumption: it is not supported by any theory. Questions about the suitability of this assumption arise by the need for a global or local stabilization. It is also worth noting that Kim and Menon[24] showed that it is well possible to use another assumption: they applied an equal-structure assumption for the SGS stress and Leonard stress L_{ij}^d. However, this assumption, too, was made on the basis of empirical indications without taking reference to any theory. Thus, existing dynamic SGS stress models cannot be seen to satisfy the property P1 of optimal models. There are also many models that do not satisfy the properties P2, P3, P4, and P5. For example, the global stabilization concept is in contradiction to properties P2, P3, and P4, and there are dynamic methods that imply a significant computational overload.[14]

Dynamic SGS stress models that have the properties P1 and P2 were obtained recently by Heinz[25] on the basis of stochastic analysis. He used a stochastic velocity model to determine stochastic solutions to the LES equation, and an implied upscaled stochastic velocity model to determine stochastic solutions to the filtered LES equation. The stochastic models can be used to calculate the SGS stress τ_{ij} and Leonard stress L_{ij}. The relation for the Leonard stress obtained

represents an equation that can be used for the calculation of dynamic model parameters. There are two main advantages of addressing this problem in terms of stochastic analysis. First, stochastic analysis allows the development of realizable SGS models.[25–29] Realizability was proven to represent a valuable guiding principle for turbulence modeling.[5,30–32] The use of realizable turbulence closure models was found to be relevant to many applications.[33–37] Second, the use of stochastic analysis can be used to systematically derive a hierarchy of transport equations, nonlinear and linear models for the SGS stress and Leonard stress.

The goal of this paper is to provide evidence that the dynamic SGS stress models proposed by Heinz[25] do also have the properties P3, P4, and P5 of optimal dynamic SGS stress models. This question was not addressed before: Ref. 25 introduced dynamic SGS stress models as implications of stochastic models without using the dynamic stress models in simulations or *a priori* analyses. The performance of dynamic SGS models obtained via stochastic analysis will be investigated here in terms of turbulent channel flow simulations.[38] Two other dynamic models will be applied for comparisons, the stabilized DSM, which is used in many applications of LES, and Wang-Bergstrom's dynamic model (WBDM),[15] which represents an extension of the DSM. The paper is organized as follows. In Sec. II, the dynamic SGS models applied in this study will be presented. Section III explains the numerical method used for performing DNS and LES. *A priori* analyses of the suitability of formulations of dynamic models and the stability properties of dynamic models will be presented in Sec. IV. The accuracy and cost of dynamic methods will be investigated in Sec. V on the basis of *a posteriori* analysis results. The conclusions of this study will be summarized in Sec. VI.

II. REALIZABLE DYNAMIC SGS MODELS

A. LES closure

To derive LES equations from the Navier-Stokes equations we define a spatial filtering operation for any variable f by

$$\widetilde{f}(\vec{x}, t) = \int G(\vec{r}) f(\vec{x} + \vec{r}, t) d\vec{r}. \tag{1}$$

Here, $G(\vec{r})$ is a filter function, which is assumed to be homogeneous. In the current study, a box filter will be applied. For the incompressible flow considered, the filtered continuity and momentum equations read

$$\frac{\partial \widetilde{U}_i}{\partial x_i} = 0, \tag{2}$$

$$\frac{\widetilde{D}\widetilde{U}_i}{\widetilde{D}t} = -\frac{1}{\rho}\frac{\partial P}{\partial x_i} + 2\nu \frac{\partial \widetilde{S}_{ik}}{\partial x_k} - \frac{\partial \tau_{ik}^d}{\partial x_k}. \tag{3}$$

Here, $\widetilde{U}_i$ refers to the filtered velocity field, $\widetilde{D}/\widetilde{D}t = \partial/\partial t + \widetilde{U}_k \partial/\partial x_k$ denotes the filtered Lagrangian time derivative, $P = \widetilde{p} + 2k/3$ is the modified filtered pressure that includes a contribution due to the SGS kinetic energy k, ρ is the constant fluid mass density, and ν is the constant kinematic viscosity. The filtered rate-of-strain tensor is defined by $\widetilde{S}_{ij} = (\partial \widetilde{U}_i/\partial x_j + \partial \widetilde{U}_j/\partial x_i)/2$. The LES equation (3) is unclosed due to the appearance of the unknown deviatoric SGS stress τ_{ij}^d, which is defined via $\tau_{ij} = \widetilde{U_i U_j} - \widetilde{U}_i \, \widetilde{U}_j$.

An attractive approach for closing the LES equation (3) is to use a stochastic turbulence model that determines stochastic solutions of the LES equations.[25–29,39–43] This means, the stochastic velocity model implies the incompressibility constraint (2), and it exactly recovers Eq. (3) for the filtered velocity. The advantage of the stochastic model is that it also provides transport equations for all the velocity moments. In particular, it can be used to derive the following transport equation

for the SGS stress τ_{ij}:[25–27,29,44]

$$\frac{\widetilde{D}\tau_{ij}}{\widetilde{D}t} + \frac{\partial T_{kij}}{\partial x_k} + \tau_{ik}\frac{\partial \widetilde{U}_j}{\partial x_k} + \tau_{jk}\frac{\partial \widetilde{U}_i}{\partial x_k} = -\frac{2}{\tau_L}\left(\tau_{ij} - \frac{2}{3}c_0 k\delta_{ij}\right). \tag{4}$$

Here, T_{kij} refers to the triple correlation tensor of SGS velocity fluctuations. Equation (4) involves two model parameters: the nondimensional parameter c_0, and the Lagrangian time scale τ_L. The parameter c_0 is related to the Kolmogorov constant C_0 by $c_0 = C_0/[C_0 + 2/3]$. An analysis reveals that $c_0 = 19/27 \approx 0.7$.[26,27,29] An analysis of the τ_L scaling shows that $\tau_L = \ell_* \Delta k^{-1/2}$, where ℓ_* has a standard value of $\ell_* = 1/3$.[26]

The solution of the SGS stress equation (4) is computationally relatively expensive. A way to reduce the computational cost is to use the stress equation (4) for the derivation of algebraic stress models. The quadratic stress model obtained in this way reads[26]

$$\tau_{ij} = \frac{2}{3}k\delta_{ij} - 2\nu_t\widetilde{S}_{ij} - C_n\Delta^2\left[\widetilde{S}_{ik}\widetilde{\Omega}_{kj} + \widetilde{S}_{jk}\widetilde{\Omega}_{ki} - 2\widetilde{S}_{ik}\widetilde{S}_{kj} + \frac{2}{3}\widetilde{S}_{nk}\widetilde{S}_{nk}\delta_{ij}\right]. \tag{5}$$

Here, $\widetilde{\Omega}_{ij} = (\partial \widetilde{U}_i/\partial x_j - \partial \widetilde{U}_j/\partial x_i)/2$ refers to the rate-of-rotation tensor, and $C_n = \ell_*^2/3$. The SGS viscosity is given by the expression $\nu_t = C_K\Delta k^{1/2}$, where $C_K = \ell_*/3$. This parametrization for ν_t was used in several applications.[5,45] However, this approach requires the solution of the equation for the SGS kinetic energy $k = \tau_{kk}/2$, which is implied by the stress equation (4). A computationally less expensive way is given by using this equation for the SGS kinetic energy to determine an equilibrium value for k. By using this value, the SGS viscosity reads $\nu_t = C_s\Delta^2|\widetilde{S}|$, where $C_s = (\ell_*/2)^2$.[26] This model corresponds to the Smagorinsky model. The use of $\ell_* = 1/3$ recovers the standard value $c_S = (1/6)^2$ for the Smagorinsky coefficient.[5,45] Only the equilibrium model $\nu_t = C_s\Delta^2|\widetilde{S}|$ will be used here for the SGS viscosity, because it was found that the use of the nonequilibrium model $\nu_t = C_K\Delta k^{1/2}$ resulted in negligible differences to the equilibrium model. Hence, the stress model considered reads

$$\tau_{ij} = \frac{2}{3}k\delta_{ij} - 2C_s\Delta^2|\widetilde{S}|\widetilde{S}_{ij} - C_n\Delta^2\left[\widetilde{S}_{ik}\widetilde{\Omega}_{kj} + \widetilde{S}_{jk}\widetilde{\Omega}_{ki} - 2\widetilde{S}_{ik}\widetilde{S}_{kj} + \frac{2}{3}\widetilde{S}_{nk}\widetilde{S}_{nk}\delta_{ij}\right]. \tag{6}$$

The quadratic stress model (6) can be reduced to a linear stress model by setting $C_n = 0$.

B. Test-filtered LES closure

The development of dynamic LES methods, which provide local values for the model parameters C_s and C_n in Eq. (6), is based on the consideration of test-filtered LES equations. The test-filtered value of any variable f is defined by

$$\overline{f}(\vec{x}, t) = \int G_T(\vec{r})f(\vec{x} + \vec{r}, t)d\vec{r}. \tag{7}$$

Here, $G_T(\vec{r})$ is a test filter function, which is assumed to be homogeneous. The test-filtering of the filtered continuity and momentum equations results in

$$\frac{\partial \overline{\widetilde{U}}_i}{\partial x_i} = 0, \tag{8}$$

$$\frac{\overline{\widetilde{D}}\,\overline{\widetilde{U}}_i}{\overline{\widetilde{D}}t} = -\frac{1}{\rho}\frac{\partial(\overline{P} + 2k^T/3)}{\partial x_i} + 2\nu\frac{\partial \overline{\widetilde{S}}_{ik}}{\partial x_k} - \frac{\partial T_{ik}^d}{\partial x_k}. \tag{9}$$

We used here $\overline{\widetilde{D}}/\overline{\widetilde{D}}t = \partial/\partial t + \overline{\widetilde{U}}_k\partial/\partial x_k$ and $\overline{\widetilde{S}}_{ij} = (\partial \overline{\widetilde{U}}_i/\partial x_j + \partial \overline{\widetilde{U}}_j/\partial x_i)/2$. The test-filtered pressure is given by $\overline{P}$, and $k^T = L_{nn}/2$ refers to the STS kinetic energy. The STS stress, which enters Eq. (9) via its deviatoric component, is defined by $T_{ij} = \overline{\widetilde{U_iU_j}} - \overline{\widetilde{U}}_i\,\overline{\widetilde{U}}_j$. The difference between T_{ij} and the test-filtered SGS stress is $L_{ij} = T_{ij} - \overline{\tau}_{ij}$. The definitions of T_{ij} and τ_{ij} reveal that the Leonard stress is defined by $L_{ij} = \overline{\widetilde{U}_i\widetilde{U}_j} - \overline{\widetilde{U}}_i\,\overline{\widetilde{U}}_j$. By accounting for Germano's identity $L_{ij} = T_{ij} - \overline{\tau}_{ij}$ we

can write Eq. (9) as

$$\frac{\overline{\overline{D}}\,\overline{\overline{U}}_i}{\overline{\overline{D}}t} + \frac{\partial L_{ik}^d}{\partial x_k} = -\frac{1}{\rho}\frac{\partial \overline{\overline{p}}}{\partial x_i} + 2\nu\frac{\partial \overline{\overline{S}}_{ik}}{\partial x_k} - \frac{\partial \overline{\tau_{ik}^d}}{\partial x_k}. \tag{10}$$

A closure of Eq. (10) can be obtained by following the approach used to close the LES Equation (3). The up-scaling of the stochastic model used to close the LES equation provides another stochastic model that implies the incompressibility constraint (8) and Eq. (9). The advantage of the stochastic model considered is that it also implies a transport equation for the STS stress L_{ij}, which is given by[25]

$$\frac{\overline{\overline{D}}L_{ij}}{\overline{\overline{D}}t} + \frac{\partial T_{kij}^T}{\partial x_k} + L_{ik}\frac{\partial \overline{\overline{U}}_j}{\partial x_k} + L_{jk}\frac{\partial \overline{\overline{U}}_i}{\partial x_k} = -\frac{2}{\tau_L^T}\left(L_{ij} - \frac{2}{3}c_0 k^T \delta_{ij}\right). \tag{11}$$

Here, T_{kij}^T is the STS triple correlation tensor of velocity fluctuations. The Lagrangian time scale at the test scale is given by $\tau_L^T = \ell_*^T \Delta^T (k^T)^{-1/2}$, where Δ^T denotes the test filter width and ℓ_*^T is a test-scale model parameter. The parameter c_0 is assumed to be unaffected by the scale.[27]

In correspondence to the derivation of Eq. (6) from Eq. (4), Eq. (11) can be used for the derivation of an algebraic stress model for L_{ij}.[25] This calculation provides

$$L_{ij} = \frac{2}{3}k^T \delta_{ij} - C_s^T\,M_{ij} - C_n^T\,N_{ij}. \tag{12}$$

Here, the matrices M_{ij} and N_{ij} are given by the expressions

$$M_{ij} = 2(\Delta^T)^2\,|\overline{\overline{S}}|\,\overline{\overline{S}}_{ij}, \tag{13}$$

$$N_{ij} = \left(\Delta^T\right)^2\left[\overline{\overline{S}}_{ik}\overline{\overline{\Omega}}_{kj} + \overline{\overline{S}}_{jk}\overline{\overline{\Omega}}_{ki} - 2\overline{\overline{S}}_{ik}\overline{\overline{S}}_{kj} + \frac{2}{3}\overline{\overline{S}}_{nk}\overline{\overline{S}}_{kn}\delta_{ij}\right]. \tag{14}$$

The model parameters are given by $C_s^T = (\ell_*^T/2)^2$ and $C_n^T = (\ell_*^T)^2/3$. In correspondence to the derivation of the algebraic stress model (6) we did only consider here the equilibrium STS viscosity. The first-order approximation for L_{ij} is obtained by setting $C_n^T = 0$ in (12).

C. Realizable dynamic SGS models

Equation (12) for L_{ij} can be used to design dynamic SGS models. First, this requires to explain how the parameters C_s^T and C_n^T in relation (12) are related to the SGS stress parameters C_s and C_n in Eq. (6). The analysis of this question shows that the test-scale coefficients C_s^T and C_n^T represent very good estimates for C_s and C_n provided that $\Delta^T < L^T$,[25] where L^T is the characteristic length scale of STS turbulent eddies. The latter condition will be considered to be given in the following. According to Eq. (12), the deviatoric component of L_{ij} is then given by

$$L_{ij}^d = -C_s^{NDM}\,M_{ij} - C_n^{NDM}\,N_{ij}, \tag{15}$$

where the superscript NDM refers to coefficients calculated by the nonlinear dynamic model. The use of any two values for C_s and C_n will result in an error of Eq. (15), which represents five conditions for C_s and C_n. This error is given by $E_{ij} = L_{ij}^d + C_s^{NDM}M_{ij} + C_n^{NDM}N_{ij}$. The quadratic error $E_{ij}E_{ji}$ becomes minimal if C_s and C_n are calculated by the relations

$$C_s^{NDM} = \frac{r_{SN}r_{LN} - r_{LS}}{1 - r_{SN}r_{SN}}\frac{|L^d|}{|M|}, \qquad C_n^{NDM} = \frac{r_{SN}r_{LS} - r_{LN}}{1 - r_{SN}r_{SN}}\frac{|L^d|}{|N|}. \tag{16}$$

Here, we used for any two symmetric matrices A and B the abbreviations $|A| = \sqrt{2A_{ij}A_{ji}}$ and

$$r_{AB} = \frac{A_{ij}B_{ji}}{\sqrt{A_{lk}A_{kl}B_{mn}B_{nm}}}. \tag{17}$$

The variable r_{AB} has the property $-1 \leq r_{AB} \leq 1$ of a correlation coefficient. The subscripts L, S, N in relations (16) refer to the use of L_{ij}^d, $\overline{\overline{S}}_{ij}$, and N_{ij}, respectively. The use of the relations (16) for providing the SGS stress parameters C_s and C_n in Eq. (6) represents the NDM.

A linearized dynamic model can be obtained by neglecting the nonlinear N_{ij} term in Eq. (15),

$$L_{ij}^d = -C_s^{LDM} M_{ij}, \tag{18}$$

where the superscript LDM refers to coefficients calculated by the linear dynamic model (LDM). The value of C_s^{LDM} that minimizes the quadratic error $E_{ij} = L_{ij}^d + C_s^{LDM} M_{ij}$ can be obtained from the relations (16) by neglecting terms involving a nonzero N_{ij},

$$C_s^{LDM} = -r_{LS} \frac{|L^d|}{|M|} = -\frac{L_{ij}^d M_{ji}}{M_{kl} M_{lk}}. \tag{19}$$

The standardized quadratic error $e = |E|^2/|L^d|^2$ for the LDM is given by the simple expression $e_{LDM} = 1 - (r_{LS})^2$.[25]

Relation (19) for the coefficient of the Smagorinsky model differs from the corresponding DSM expression (A3) given in Appendix A. The DSM expression was obtained by combining Germano's identity $L_{ij}^d = T_{ij}^d - \overline{\tau_{ij}^d}$ with the assumption $T_{ij}^d = -C_s^{DSM} M_{ij}$ for the deviatoric STS stress, which leads to $L_{ij}^d = -C_s^{DSM} H_{ij}$ instead of $L_{ij}^d = -C_s^{LDM} M_{ij}$ applied here (H_{ij} is defined in Appendix A by Eq. (A2)). The latter two relations for L_{ij}^d have different support: $L_{ij}^d = -C_s^{DSM} H_{ij}$ suggested by Germano is based on an assumption for T_{ij}^d, whereas $L_{ij}^d = -C_s^{LDM} M_{ij}$ was derived by stochastic analysis.[25] It is interesting to note that Fabre and Balarac[46] suggested a similar modification of Germano's approach regarding the dynamic modeling of the SGS scalar flux based on Taylor series expansions. In correspondence to the use of the same approach for the modeling of both the SGS stress τ_{ij} and Leonard stress L_{ij} here, Fabre and Balarac[46] found it to be very beneficial to apply the same approach to model both the SGS scalar flux and the corresponding Leonard-type scalar flux.

III. NUMERICAL METHOD

A sketch of the computational domain is shown in Fig. 1. The domain size $(L_x * L_y * L_z)$ is taken to be $(2\pi * 2 * \pi)$ according to the DNS of Moser et al.[38] All simulations were performed for a friction Reynolds number $Re_\tau = u_\tau \delta/\nu = 395$. Here, $u_\tau = \sqrt{\tau_w/\rho}$ is the friction velocity, τ_w refers to the wall shear stress, and δ is the half channel width. This Reynolds number was chosen to enable efficient DNS of a flow that is not significantly affected by Reynolds number effects.

DNS and LES were performed by using the OpenFOAM CFD Toolbox.[47] The dynamic LES models have been implemented inside the OpenFOAM CFD Toolbox. The calculations have been performed by using a finite-volume based method. The convection term in the momentum equation was discretized using a second-order central difference scheme. The pressure gradient that drives the flow in the channel has been adjusted dynamically to maintain a constant mass flow rate. The
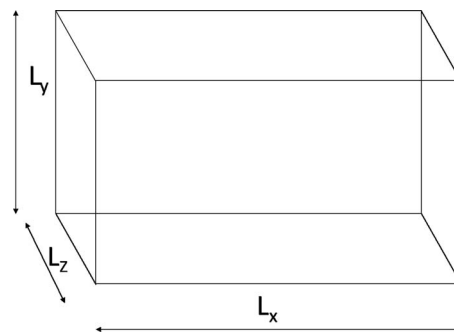

FIG. 1. The domain considered: $(L_x * L_y * L_z) = (2\pi * 2 * \pi)$ according to the DNS of Moser et al.[38]

PISO algorithm was used for the pressure-velocity coupling.[48] The resulting algebraic equation for all the flow variables except pressure has been solved iteratively using a preconditioned bi conjugate gradient method with a diagonally incomplete LU preconditioning at each time step. The Poisson equation for the pressure was solved using an algebraic multi-grid solver. When the scaled residual became less than 10^{-6}, the algebraic equation was considered to be converged. Time marching was performed using a second-order backward difference scheme. The time step was modified dynamically to ensure a constant Courant-Friedrichs-Lewy (CFL) number of 0.5. Periodic boundary conditions have been employed along the streamwise and spanwise direction for all the flow variables. Along the wall normal direction, a no slip boundary condition was employed for the velocity and a zero gradient boundary condition has been used for the pressure term.

A uniformly distributed grid was used along the streamwise and spanwise directions while the grid was refined in the wall normal direction using a hyperbolic tangent function. The DNS were performed on a grid size of $384 * 256 * 256$. A much higher grid resolution was used compared to the simulations of Moser et al.[38] ($256 * 193 * 192$) because the current study uses a lower-order finite difference scheme while the simulations of Moser et al. used a spectral code. Based on the recommendation of Gullbrand and Chow,[49] the LES were performed on a grid size of $81 * 64 * 81$. This grid size was suggested by Gullbrand and Chow[49] to minimize the effect of numerical errors arising from second-order schemes. The numerical grid with a filter width $\Delta = (\Delta_x \Delta_y \Delta_z)^{1/3}$ was used as LES filter.

To assess the effect of the initial conditions on the stability of the numerical calculations and results we considered three inflow generation methods: (i) the addition of uncorrelated sinusoidal velocity fluctuations (which satisfy the incompressibility constraint) to a laminar flow field, (ii) the addition of uncorrelated sinusoidal velocity fluctuations (which satisfy the incompressibility constraint) to the flow field obtained from a RANS channel flow simulation using the $k - \omega$ model of Bredberg et al.,[50] and (iii) the use of an unsteady flow field obtained from a coarse grid ($32 * 64 * 32$) channel flow simulation using the Smagorinsky model combined with a Van Driest's wall damping function.[51] We observed that simulations using the dynamic SGS models considered here (including the linear and nonlinear dynamic models described in Sec. II C combined with a transport equation for k) remained stable for all the three methods and that the computed statistics were independent of the initial conditions.

The OpenFOAM DNS results were compared with the DNS data of Moser et al.[38] to ensure that the grid resolution used for the OpenFOAM DNS was appropriate. Figures 2(a) and 2(b) show the corresponding comparison of the normalized mean streamwise velocity and normalized Reynolds shear stress. The agreement between the two DNS is excellent, which shows that the OpenFOAM DNS resolution is sufficient. The same conclusion is obtained regarding the comparison of the normalized Reynolds normal stress components and turbulent kinetic energy: see Fig. 3.
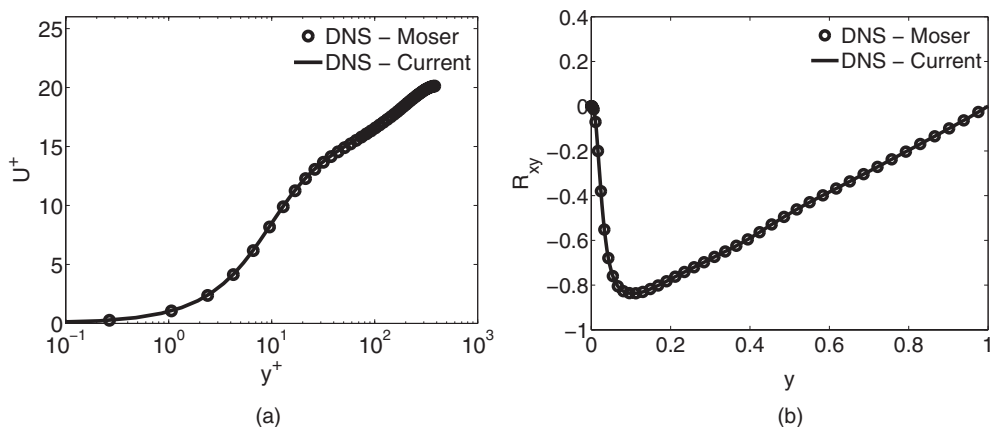

FIG. 2. OpenFOAM DNS and DNS data of Moser et al.:[38] (a) Normalized mean streamwise velocity $U^+ = U_1/u_\tau$, (b) Reynolds shear stress normalized by u_τ^2.
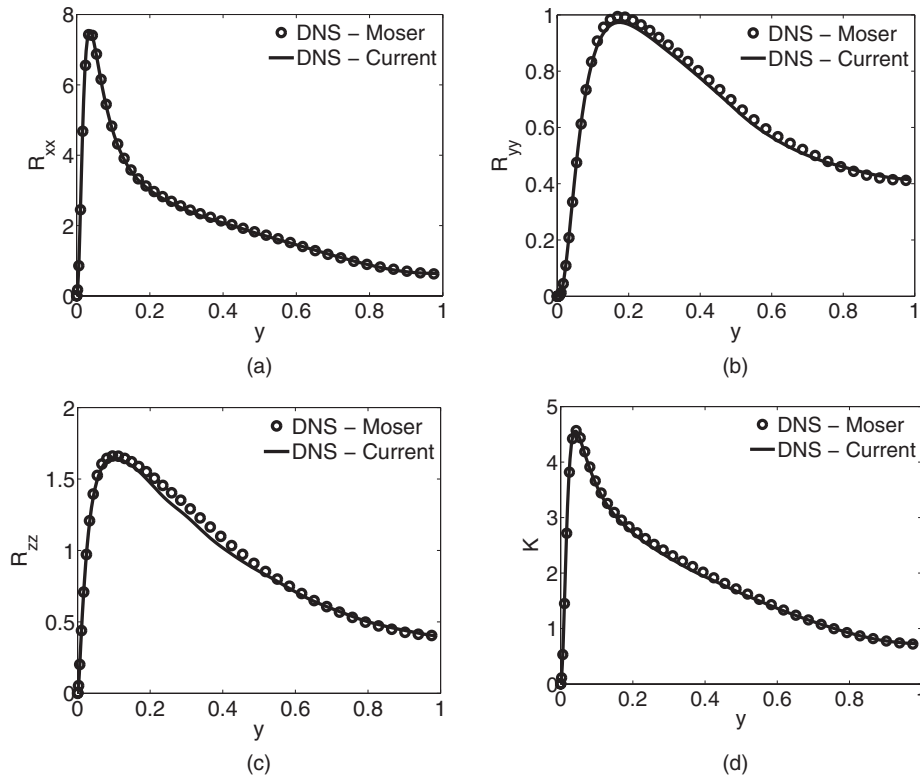
FIG. 3. OpenFOAM DNS and DNS data of Moser *et al.*:[38] Reynolds streamwise normal stress (a), wall-normal stress (b), spanwise normal stress (c), and turbulent kinetic energy K (d) normalized by u_τ^2.

A priori analyses were used to compare exact SGS quantities obtained from DNS with SGS quantities obtained from different dynamic methods. Ten realizations of the DNS simulations were saved to perform these analyses. To ensure that the flow fields were uncorrelated, the time interval between each realization was set equal to six eddy turnover times L_x/U_b, where U_b is the bulk velocity. By using box filtering, filtered values $\widetilde{f}$ and test filtered values $\widetilde{\widetilde{f}}$ of any variable f were obtained according to

$$\widetilde{f} = \int_{z-\Delta}^{z+\Delta} \int_{x-\Delta}^{x+\Delta} f(x, y, z)dxdz, \tag{20}$$

$$\overline{\widetilde{f}} = \int_{z-r\Delta/2}^{z+r\Delta/2} \int_{x-r\Delta/2}^{x+r\Delta/2} \widetilde{f}(x, y, z)dxdz, \tag{21}$$

where $r = \Delta^T/\Delta$. The filtering and test filtering are illustrated in Fig. 4. The dots refer to instantaneous velocity data available at positions separated by Δ in a homogeneous direction. The solid box in Fig. 4(a) illustrates the calculation of the filtered variables $\widetilde{f}(i)$ at the midpoint i of the solid box by $\widetilde{f}(i) = [f(i-1) + 2f(i) + f(i+1)]/4$, where $f(i-1)$ and $f(i+1)$ refer to the values at the left and right corners of the box, respectively. Test filtered variables are calculated correspondingly for the $r = 2$ case. The dashed box in Fig. 4(a) illustrates a moving filtering, this means the same procedure is applied to all (except the first and last) points in the direction considered. Once the filtered (or $r = 2$ test filtered) velocities at all points considered are known, velocity gradients are calculated by the difference of the values at the left and right ends of the box, corresponding to a second-order central difference scheme. The calculation of test filtered variables for $r = 1$, which is illustrated in the right-hand side picture of Fig. 4, is performed correspondingly. The only difference is that the values at the ends of boxes are calculated by interpolating the data available at $\pm \Delta/2$. All (except

FIG. 4. Illustration of filtering and test filtering over 2Δ (left-side) and Δ (right-side).

instantaneous) data shown below along the wall-normal direction are averaged over homogeneous directions and the ten realizations of the DNS simulations considered.

IV. *A PRIORI* ANALYSIS

The suitability of dynamic SGS models will be evaluated in this section by the analysis of DNS data. Two essential questions will be addressed. First, we consider various correlation coefficients and model errors to see which dynamic concept provides the more appropriate equation used for the dynamic calculation of model parameters. Second, the probability density function (PDF) of dynamic model parameters and the backscatter implied by several dynamic methods will be considered to derive conclusions about the computational stability properties of dynamic methods. In particular, there is the question about the differences between the DSM (which leads to computational instabilities), the extension of the DSM given by the WBDM, and the linear and nonlinear dynamic models derived from stochastic analysis, this means the LDM and NDM.

A. Dynamic model formulation

First of all, the difference between dynamic LES methods is given by the equation that determines dynamic model parameters. Two concepts were considered in Sec. II: Germano's approach, which assumes $L_{ij}^d = -C_s^{DSM} H_{ij}$ for the calculation of C_s, and the calculation of C_s via $L_{ij}^d = -C_s^{LDM} M_{ij}$, which was derived by Heinz[25] on the basis of stochastic analysis. The suitability of these parametrizations of L_{ij}^d can be assessed by calculating r_{LH} and r_{LM}, which reflect the degree of correlation between L_{ij}^d and H_{ij} and L_{ij}^d and M_{ij}, respectively. The coefficient $r_{LM} = r_{LS}$, as may be seen in terms of the definition of M_{ij}. The coefficients r_{LH} and r_{LS} determine the standardized quadratic errors $e = |E|^2/|L^d|^2$ given by $e_{DSM} = 1 - (r_{LH})^2$ for the DSM and $e_{LDM} = 1 - (r_{LS})^2$ for the LDM: see Sec. II and Appendix A. Hence, the suitability of different calculations of dynamic model parameters can be evaluated by considering e_{DSM} and e_{LDM}. Interestingly, the errors e_{DSM} and e_{LDM} can be calculated at every instant of time during the numerical simulations, this means these errors can be used for the uncertainty quantification of simulations.

The corresponding variations of e_{DSM} and e_{LDM}, which are averaged over homogeneous directions and the ten DNS realizations considered, are shown in Fig. 5(a) along the wall-normal direction. The cases $r = \Delta^T/\Delta = 1$ and $r = 2$ are considered. The case $r = 2$ represents the standard setting for r. The case $r = 1$ is used as a reference case to see the effect of r variations on dynamic models. This case is also of interest regarding the approximation of test-scale coefficients C_s^T and C_n^T by C_s and C_n (see Sec. II C): compared to $r = 2$, it may be expected that this assumption is more appropriate for $r = 1$. It is surprising to see that the variation of r does hardly have any influence on the DSM results. The correlation between L_{ij}^d and H_{ij} is small ($r_{LH} = 0.2$ over most of the channel) leading to a high normalized DSM error $e_{DSM} = 0.96$. These observations do not provide much support for the basic assumption of Germano's approach that L_{ij}^d and H_{ij} are proportional to each other. On the other hand, the proportionality between L_{ij}^d and M_{ij} used in the LDM has a much higher level of support. We find $e_{LM} < e_{LH}$ over all the channel. Away from the near-wall region r_{LM} approaches $r_{LM} = 0.5$ corresponding to $e_{LDM} = 0.75$. This correlation value is 2.5 times higher than the corresponding value $r_{LH} = 0.2$ obtained for the DSM. The significant model error reduction obtained for the LDM clearly indicates potential advantages of the LDM concept compared to the DSM concept.

Figure 5(b) compares the LDM error with the corresponding errors of the nonlinear NDM and WBDM models for $r = 2$. It may be seen that the use of both nonlinear models leads to a
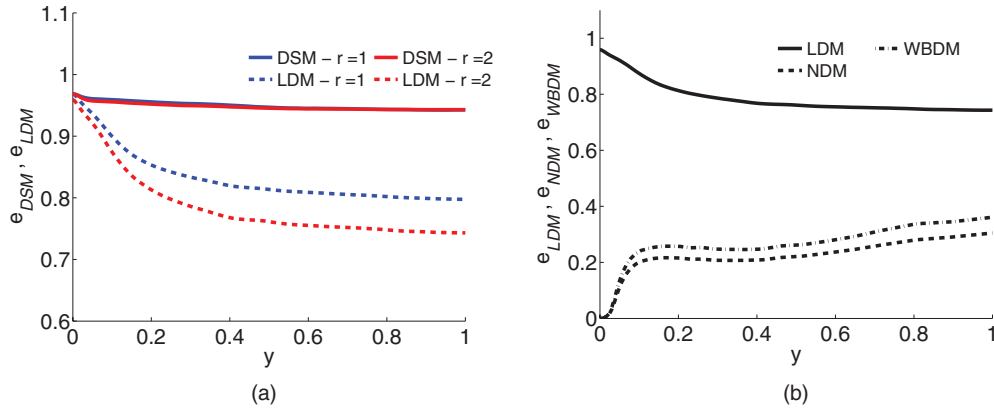
FIG. 5. The standardized error $e = [|E|/|L^d|]^2$ of the DSM and LDM is shown in (a) for $r = \Delta^T/\Delta = 1$ and $r = 2$. The LDM error is compared to the errors of the nonlinear NDM and WBDM for $r = 2$ in (b).

significant model error reduction. The variation of the model error along the wall-normal direction is very similar. It may be also seen that the NDM performs better than the WBDM. However, the difference is relatively little, indicating that the accuracy of both models observed in simulations will be comparable.

Further insight into the suitability of the DSM and LDM dynamic stress concepts can be obtained by comparing a modeled variable A_{ij}^M (e.g., the SGS stress) with the corresponding exact variable A_{ij}^E, which is determined by the definition of the variable considered. This will be done next by using the matrix correlation coefficient

$$R_A = \frac{\langle A_{ij}^M A_{ji}^E \rangle}{\langle A_{kl}^M A_{lk}^M \rangle^{1/2} \langle A_{mn}^E A_{nm}^E \rangle^{1/2}}. \tag{22}$$

The bracket symbol $\langle \cdots \rangle$ refers to averaging in time and homogeneous directions in space. By following the analysis of correlation coefficients one can show that $-1 \leq R_A \leq 1$. It is worth noting that the matrices A_{ij}^M and A_{ij}^E do not have to represent fluctuations. This approach will be used in the following with regard to:

(1) The deviatoric STS stress L_{ij}^d, i.e., by considering $A_{ij}^E = \overline{\widetilde{U}_i \widetilde{U}_j} - \overline{\widetilde{U}}_i \, \overline{\widetilde{U}}_j - (\overline{\widetilde{U}_k \widetilde{U}_k} - \overline{\widetilde{U}}_k \, \overline{\widetilde{U}}_k) \, \delta_{ij} /3$ and $A_{ij}^M = -C_s^{DSM} H_{ij}$ for the DSM and $A_{ij}^M = -C_s^{LDM} M_{ij}$ for the LDM. This correlation coefficient will be denoted by R_L.

(2) The deviatoric SGS stress τ_{ij}^d, i.e., by considering $A_{ij}^E = \widetilde{U_i U_j} - \widetilde{U}_i \widetilde{U}_j - (\widetilde{U_k U_k} - \widetilde{U}_k \widetilde{U}_k) \, \delta_{ij} /3$ and $A_{ij}^M = -2C_s^{DSM} \Delta^2 |\widetilde{S}| \widetilde{S}_{ij}$ for the DSM and $A_{ij}^M = -2C_s^{LDM} \Delta^2 |\widetilde{S}| \widetilde{S}_{ij}$ for the LDM. This correlation coefficient will be denoted by R_τ.

(3) The kinetic energy production $-\tau_{ij}^d \widetilde{S}_{ij}$. Here, A_{ij}^E and A_{ij}^M reduce to scalars. The exact and model values of A_{ij}^E and A_{ij}^M are given by using the exact and modeled SGS stress, see Sec. II. This correlation coefficient will be denoted by R_P.

Here, the dynamic constant C_s is calculated by Eq. (A3) for the DSM and Eq. (19) for the LDM.

For the DSM and LDM, the corresponding plots of R_L, R_τ, and R_P are shown in Figs. 6(a), 6(c), and 6(e), respectively, for $r = 1$ and $r = 2$. There are two relevant conclusions. First, the use of $r = 2$ improves significantly the correlations considered compared to the $r = 1$ case. Second, compared to the DSM the LDM provides consistently significantly higher correlations. The latter fact provides again support for the view that the stochastic analysis concept used to derive the LDM is a more appropriate concept than Germano's dynamic model concept. It is interesting to observe that the $r = 2$ values of the correlation coefficient R_P are very high, indicating that the LDM represents the instantaneous production of turbulent kinetic energy, which is the most important consequence of a SGS stress model, very well.
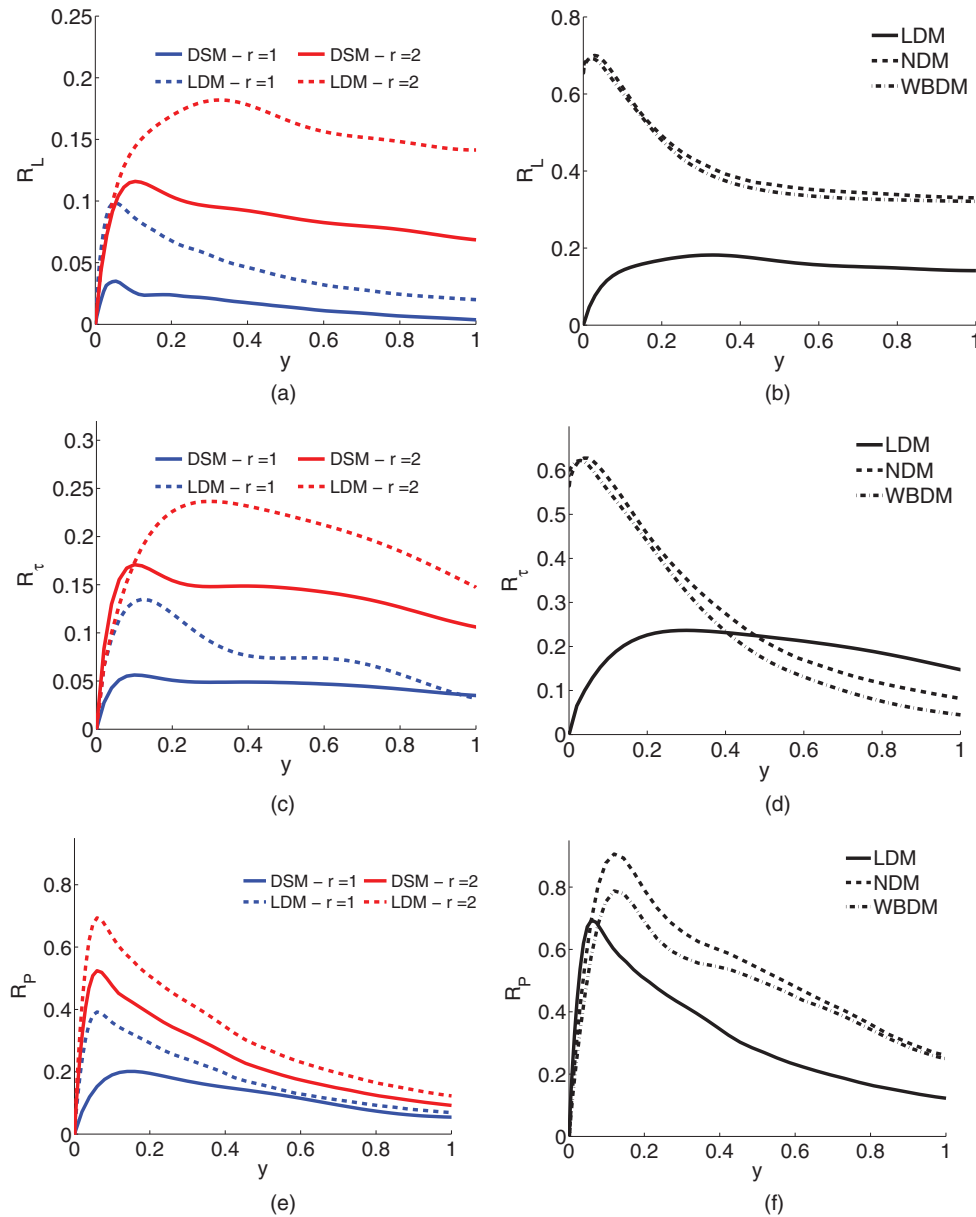
FIG. 6. Correlation coefficients defined in Sec. IV A. Results for the DSM and LDM are shown for $r = 1$ and $r = 2$ in (a), (c), and (e). The other plots show results obtained for the NDM and WBDM for $r = 2$.

This comparison can be extended to the inclusion of the nonlinear NDM and WBDM models by using the SGS and STS stresses implied by these models: see Sec. II C. The corresponding results are shown for $r = 2$ in Figs. 6(b), 6(d), and 6(f). It may be seen that both nonlinear models provide significantly higher correlations compared to the linear models. This concerns, in particular, the R_L and R_τ values. It may be also seen that the NDM always provides slightly higher correlation values than the WBDM, which represents an extension of Germano's dynamic concept. Therefore, these results, too, provide support for the benefits of dynamic methods based on stochastic analysis.

B. Stability properties of dynamic models

Next, let us have a closer look at the differences of dynamic SGS models regarding the variation of dynamic constants and their implied PDFs, and at the differences of backscatter implied by the
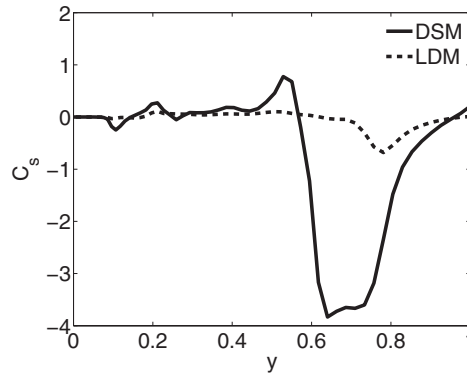
FIG. 7. Instantaneous values of the dynamic constant C_s along $(\pi, y, \pi/2)$ for the DSM and LDM obtained from *a priori* analysis, where $r = \Delta^T/\Delta = 2$.

various models. These discussions are helpful to obtain a better insight into the stability properties of dynamic SGS models.

Instantaneous local values of C_s obtained by the DSM and LDM are shown for $r = 2$ in Fig. 7 along the wall-normal direction at a streamwise and spanwise location of $x = \pi$ and $z = \pi/2$. The C_s^{DSM} value represents the original DSM value calculated by expression (A3). This figure shows that there are significant fluctuations of C_s^{DSM}. On the other hand, the C_s^{LDM} curve is much smoother and shows a much smaller range of variations. The C_s^{DSM} and C_s^{LDM} values represent constants of proportionality in their constant-determining relations $L_{ij}^d = -C_s^{DSM} H_{ij}$ and $L_{ij}^d = -C_s^{LDM} M_{ij}$, respectively. Figure 7 indicates, therefore, that the consideration of $L_{ij}^d = -C_s^{LDM} M_{ij}$, which was obtained by stochastic analysis, is a more appropriate concept. This figure also provides support for the explanation of the reason for the DSM instability by Lund *et al.*:[13] The C_s^{DSM} values are found to be negative in an extended channel flow region (for about $0.56 < y < 0.96$), which can cause a divergence of the total energy due to the exponential growth of the local velocity fields implied by a negative eddy viscosity.

A much more complete view of the behavior of dynamic constants is obtained by looking at the PDF of C_s or the logarithm of this PDF. These plots are shown in Fig. 8 at $y^+ = 40$ (corresponding to $y = 0.1$) for $r = 2$. Here, $y^+ = u_\tau d_y/\nu$ is the dimensionless wall distance, where d_y refers to the wall distance. The PDFs were calculated by using $20(N_x - 2)(N_z - 2)$ samples, where $N_x = 384$ and $N_z = 256$. This number of almost 2×10^6 samples is sufficient for the calculation of PDFs which are basically unaffected by the number of samples applied.[44] A filter size of 0.1 was used for the PDF
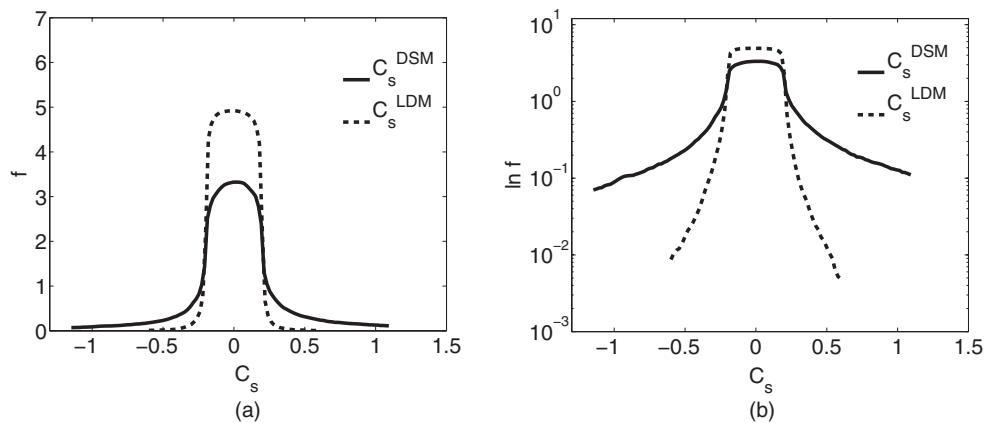

FIG. 8. Comparison of the PDF of C_s obtained for the DSM and LDM: (a) PDF, (b) PDF logarithm, where $r = \Delta^T/\Delta = 2$. The PDFs were calculated for the horizontal slice at $y^+ = 40$.
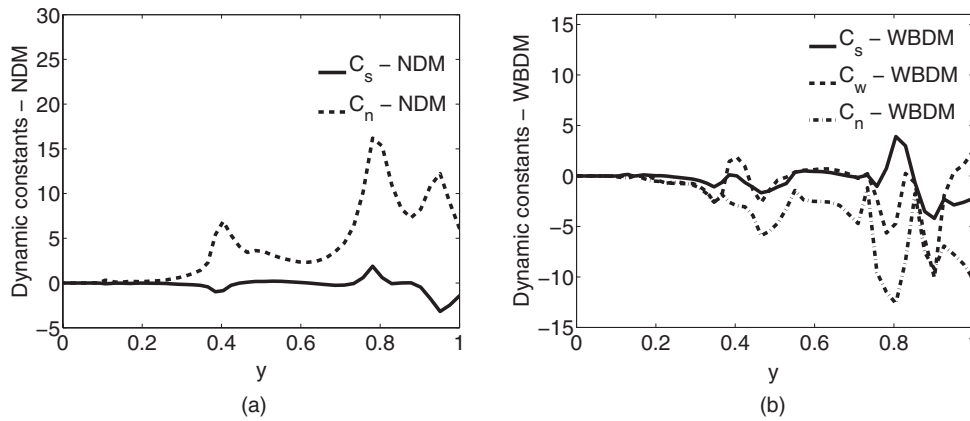
FIG. 9. Realizations of the dynamic constants along $(\pi, y, \pi/2)$ obtained from *a priori* analysis for $r = 2$: (a) NDM, (b) WBDM.

calculation. It is interesting to observe that the C_s^{LDM} PDF shape is relatively close to a uniform PDF shape, which appears to be reasonable. A relevant conclusion is that the stochastic modeling concept provides (without the use of any empirical clipping procedure) a natural clipping of dynamic constant values. The significantly different behavior of the C_s^{DSM} PDF can be seen by looking at the logarithm of this PDF. It can be observed that the probability of very high positive or negative C_s^{DSM} values can be by two orders of magnitude higher than the corresponding probability for finding corresponding C_s^{LDM} values. The nonzero probability for very high negative C_s^{DSM} values explains the DSM trend to become computationally unstable.

Realizations of the dynamic model parameters of the NDM (C_s^{NDM} and C_n^{NDM}) and WBDM (C_s^{WBDM}, C_w^{WBDM}, and C_n^{WBDM}) are shown for $r = 2$ along the wall-normal direction in Fig. 9. Corresponding PDF plots are shown at $y^+ = 40$ in Fig. 10. It may be seen that the variations of dynamic model parameters are much higher than the variations of linear dynamic model parameters. For nonlinear models, the signs of model parameters cannot be used to derive conclusions regarding the computational stability of models, which is the result of the complex interaction of different linear and nonlinear terms in the stress relations applied. Regarding the NDM we see an interaction of positive and negative coefficients of the linear stress contribution with positive and relatively large coefficients of the nonlinear stress contribution. It is very interesting to see that the WBDM is characterized by similar features. The C_s^{WBDM} and C_w^{WBDM} PDFs compare well with the C_s^{NDM} PDF, and the C_n^{WBDM} PDF compares well with the C_n^{NDM} PDF. C_n^{WBDM} has the opposite sign of
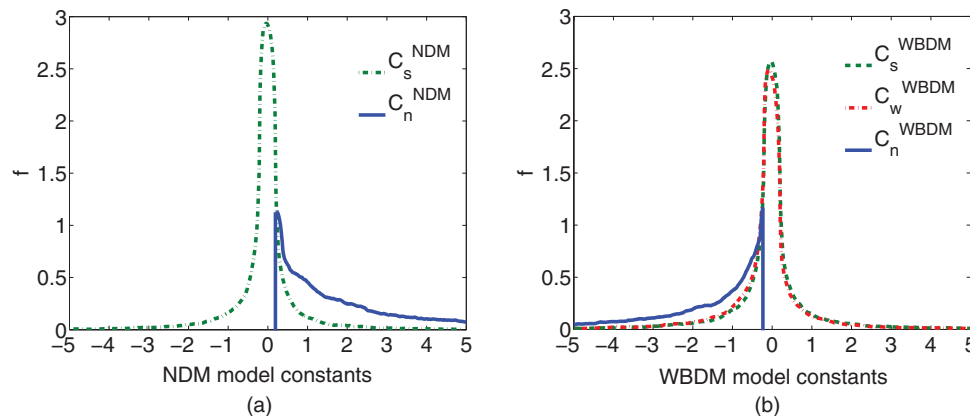

FIG. 10. PDFs of the dynamic constants of nonlinear models for $r = 2$: (a) NDM, (b) WBDM. The PDFs were calculated for the horizontal slice at $y^+ = 40$.

C_n^{NDM} because the corresponding terms in the NDM and WBDM are formulated with different signs. There are two essential differences between the NDM and WBDM. First, the WBDM does not combine the first two contributions in Eq. (14) with the squared strain-rate terms, but these terms are considered separately, which corresponds to the introduction of C_w^{WBDM}. Second, the WBDM follows Germano's approach for setting up the dynamic procedure. The second difference may be expected to be less relevant regarding the fact that both the NDM and WBDM are capable of ensuring the stability of simulations due to their inclusion of several dynamic model parameters. Figure 10 supports the view that the first two contributions in Eq. (14) have a relatively minor influence on the dynamic method because the C_n^{NDM} and C_n^{WBDM} PDFs are very similar. A consequence of this view is that dynamic C_w^{WBDM} variations will have little influence on the stabilization mechanism of nonlinear dynamic models, which is consistent with the fact that the simpler NDM can ensure computational stability: see Sec. V. Thus, the introduction of the dynamic C_w^{WBDM} (which is found to be hardly correlated to C_s^{WBDM}: the correlation coefficient between C_w^{WBDM} and C_s^{WBDM} is equal to 0.08 at $y^+ = 40$) corresponds to the consideration of an additional noise source in dynamic calculations. Support for this view is provided by Fig. 9(b), which shows that the variability of the dynamic WBDM parameters along the wall-normal direction is considerably higher than the variability of the dynamic NDM parameters.

The consideration of backscatter features of dynamic models can also contribute to the explanation of computational stability features of models. The mean backscatter is defined by $P_B = \langle P - |P| \rangle / 2$, where the kinetic energy production is given by $P = -\tau_{ij}^d \widetilde{S}_{ij}$. By definition, backscatter measures the amount of negative energy production, this means the transfer of energy from the smaller scales to the larger scales.[52]

The backscatter properties of the linear DSM and LDM models are compared with DNS data in Fig. 11(a) for $r = 1$ and $r = 2$. The DSM significantly overpredicts the DNS backscatter for $r = 1$. For $r = 2$, the DSM backscatter does also overpredict the DNS backscatter in the near-wall region. This observation is in consistency with the high DSM model error and the significant fluctuations of C_s^{DSM}: see Figs. 5(a) and 8(a), respectively. A dynamic stress model will promote computational instabilities if the amount of modeled backscatter is higher than the DNS backscatter. These facts provide an explanation for the numerical instability of the DSM seen in simulations. The backscatter provided by the LDM is rather small for $r = 1$ and significantly improved for $r = 2$. The relevant fact is that the LDM backscatter underpredicts the DNS backscatter which avoids the development of computational instabilities. Hence, this backscatter analysis does also show that the LDM has advantages compared to the DSM.

A comparison of the backscatter properties of the nonlinear NDM and WBDM models with DNS data and the LDM results is shown in Fig. 11(b) for $r = 2$. It may be seen that both nonlinear models provide a significant improvement compared to the LDM, but such that the backscatter is
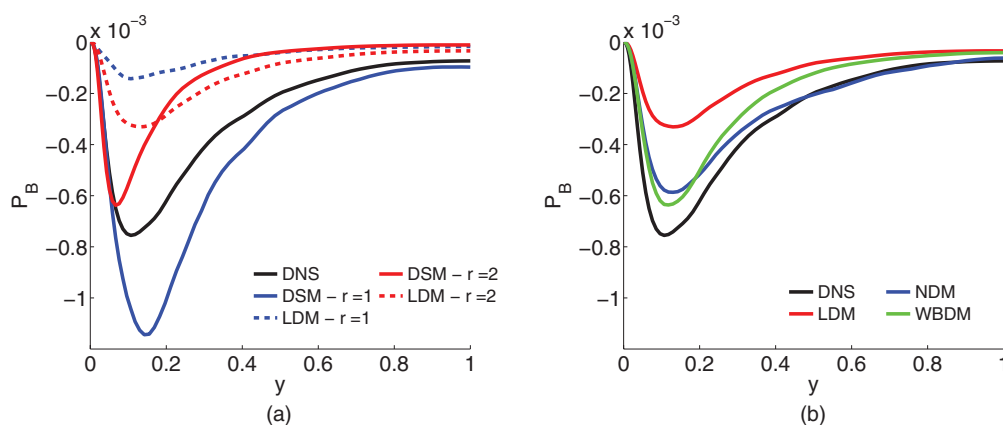

FIG. 11. The DNS backscatter is compared in (a) with the backscatter of the DSM and LDM for $r = 1$ and $r = 2$. In (b), the DNS backscatter is compared with the backscatter of the LDM, NDM and WBDM for $r = 2$.

below the DNS backscatter. Correspondingly, the NDM and WBDM are found to be computationally stable in simulations: see Sec. V. The peak value of the NDM backscatter is slightly below the peak value of the WBDM. On the other hand, the NDM backscatter approaches the DNS backscatter away from the wall in difference to the behavior of the WBDM.

V. *A POSTERIORI* ANALYSIS

Next, we will discuss the application of linear and nonlinear dynamic methods in simulations. To enable stable simulations with the DSM, the coefficient C_s^{DSM} was locally averaged along the cell faces and numerically clipped, this means C_s^{DSM} was set to zero when it became negative to avoid numerical instabilities. The LDM, NDM, and WBDM were used without any modification of dynamic coefficients. The results of the non-equilibrium LDM and NDM versions, which provide the SGS kinetic energy via a transport equation,[25] are not included because these results were found to be in an excellent agreement with the LDM and NDM, respectively. It is worth noting that the application of the non-equilibrium LDM and NDM versions did not cause any computational stability problems.

A. Accuracy

The accuracy of *a posteriori* results obtained with the dynamic models considered is compared with DNS data in Figs. 12 and 13. The comparison of profiles of the mean streamwise velocity and resolved Reynolds shear stress shows that the DSM, LDM, WBDM, and NDM results agree very well with the DNS data. Compared to the DNS results, all the models slightly underpredicted the coefficient of skin-friction $C_f = \tau_w/(0.5\rho U_b^2)$ by about 5%. The comparison of the resolved Reynolds normal stresses and resolved turbulent kinetic energy in Fig. 13 shows a very good agreement between the predictions of the various dynamic models. For all the cases, the streamwise resolved Reynolds normal stress is slightly overpredicted compared to the DNS data. This causes an underprediction of the wall normal and spanwise components of the Reynolds normal stresses. Corresponding results were also obtained in previous studies using second-order central difference schemes.[49] This slightly inaccurate representation of the energy distribution causes a slight overprediction of the resolved turbulent kinetic energy. However, the error of the peak value prediction of the resolved turbulent kinetic energy obtained by the different dynamic methods is found to be less than 10%.

Compared to the non-stabilized and stabilized DSM, the advantage of the LDM is that this model enables stable simulations without clipping or averaging of the dynamic constant. The dynamic constant C_s^{LDM} in the LDM can take on positive and negative values, which is relevant to the inclusion of backscatter. An illustration of typical variations of C_s^{LDM} is given in Fig. 14. To understand the
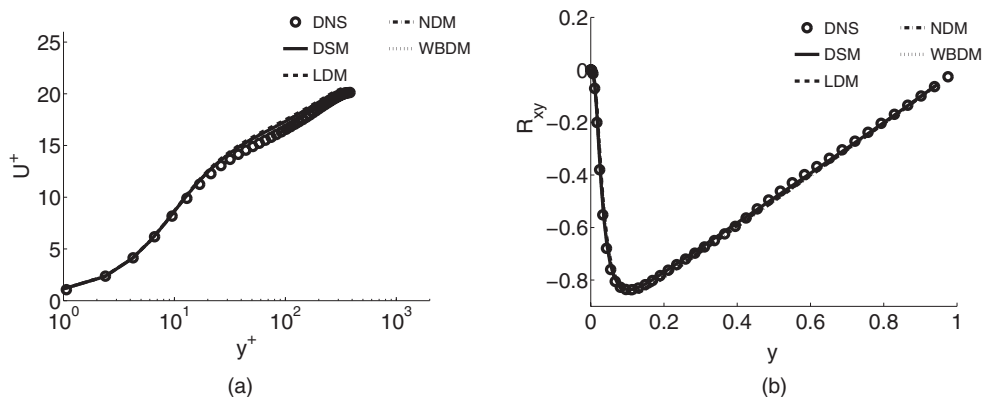

FIG. 12. *A posteriori* DSM, LDM, NDM, and WBDM results for $r = 2$ in comparison with DNS: (a) mean streamwise velocity, (b) resolved Reynolds shear stress.
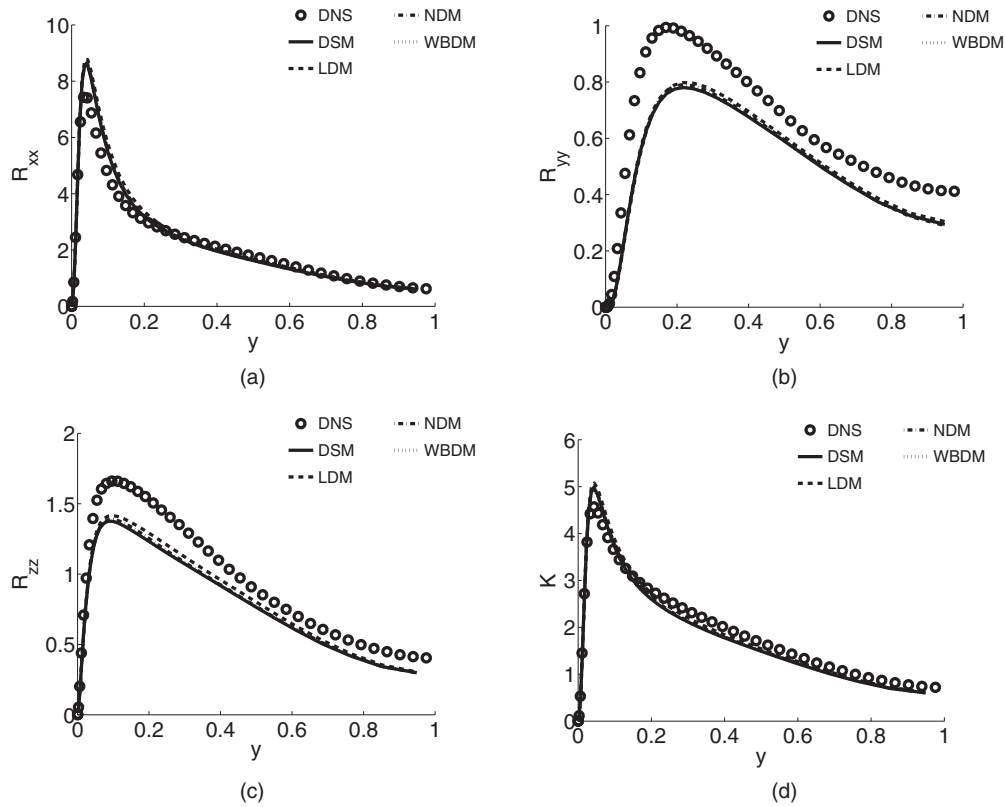
FIG. 13. *A posteriori* DSM, LDM, NDM, and WBDM results for $r = 2$ in comparison with DNS: (a) resolved Reynolds streamwise normal stress, (b) resolved Reynolds wall-normal stress, (c) resolved Reynolds spanwise normal stress, and (d) resolved turbulent kinetic energy.

effect of the stabilization procedure used for the DSM, contour plots of the instantaneous normalized streamwise velocity $U^+ = U_1/u_\tau$ obtained for the stabilized DSM and LDM will be compared with DNS data at $y^+ = 5$ and $y^+ = 50$, respectively. The comparison at $y^+ = 5$ is helpful for the evaluation of the performance of dynamic models in the near-wall region, where all the turbulence is generated. The value $y^+ = 50$ corresponds to the location of the first grid point above the wall for the case that high Reynolds number LES combined with wall-functions is performed on coarse grids (such simulations are used for LES studies of the atmospheric boundary layer). Instantaneous streamwise velocity plots obtained by using the nonlinear NDM and WBDM are not shown because these plots are very similar to the LDM plots.

The DNS results at $y^+ = 5$ presented in Fig. 15(a) show long elongated structures. These streaks agree with the structures observed in previous DNS simulations of turbulent channel flow.[53] At
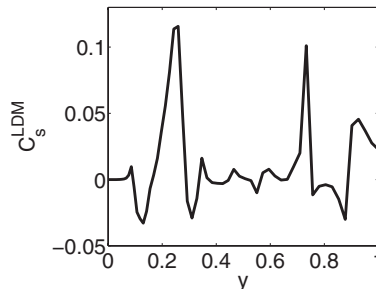

FIG. 14. A realization of the dynamic LDM constant C_s^{LDM} for $r = 2$ at the location $(\pi, y, \pi/2)$.
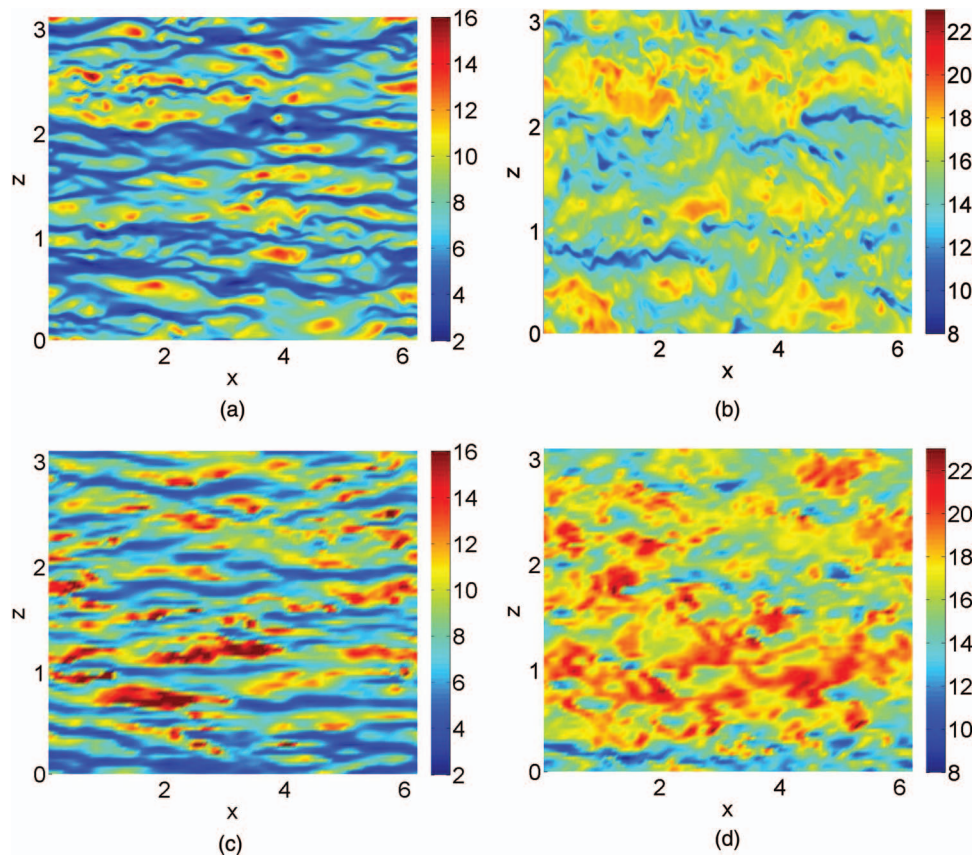
FIG. 15. Instantaneous streamwise velocity contours at $y^+ = 5$ (left-hand side pictures) and $y^+ = 50$ (right-hand side pictures) obtained for DNS (upper row) and DNS on the $81 * 64 * 81$ grid used for performing LES (lower row).

$y^+ = 50$ the length of the streaks is reduced and the organized streaky pattern seen for $y^+ = 5$ disappeared. Instead, Fig. 15(b) indicates the existence of three-dimensional turbulence structures covering a range of scales.[54] To see the relevance of SGS stress modeling, the DNS results are compared in Figs. 15(c) and 15(d) with results of simulations that do not apply a SGS stress model, which means DNS on the $81 * 64 * 81$ grid used for performing LES. It may be seen that the neglect of the SGS stress model implies a significant overprediction of instantaneous streamwise velocities. The comparison of Figs. 15(b) and 15(d) shows that turbulence structures are merged to larger-scale structures if no SGS stress model is applied. Therefore, the neglect of a SGS stress model results in significant shortcomings regarding the representation of small-scale turbulence dynamics. The LDM results shown in Figs. 16(a) and 16(b) agree very well with the DNS results for both $y^+ = 5$ and $y^+ = 50$. For $y^+ = 5$ we observe elongated streaks, and the same three-dimensional turbulence structures as seen in DNS are visible for $y^+ = 50$. Compared to the DNS, the LDM results reveal a minor overprediction of the streamwise velocity. The DSM results shown in Figs. 16(c) and 16(d) for $y^+ = 5$ and $y^+ = 50$ differ from the DNS results. For $y^+ = 5$, Fig. 16(c) does not show clearly visible streaky structures, and the streamwise velocity is underpredicted. For $y^+ = 50$, Fig. 15(d) reveals a significant overprediction of instantaneous streamwise velocities. The turbulence structures are smeared out and merged to large-scale structures, this means the small-scale structure of turbulence is not well represented. The reason for these shortcomings of the DSM is given by the stabilization procedure applied: the averaging and clipping involved does not enable the simulation of backscatter. Therefore, the use of the LDM is definitely a better choice than the application of the DSM. The LDM involves backscatter which enables an accurate representation of small-scale turbulence, and it is capable of correctly representing the typical streaky structures seen in the near-wall region of wall-bounded flows.
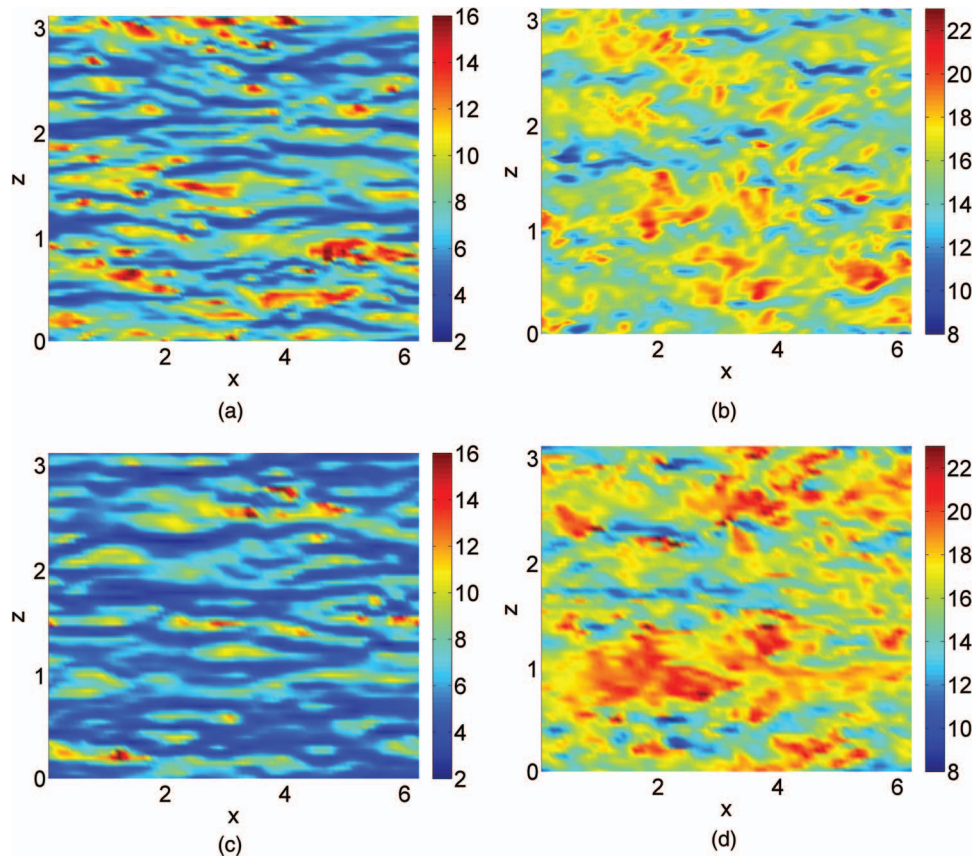
FIG. 16. Instantaneous streamwise velocity contours at $y^+ = 5$ (left-hand side pictures) and $y^+ = 50$ (right-hand side pictures) obtained for the LDM (upper row) and DSM (lower row).

B. Cost

Finally, the computational efficiency of the different dynamic models will be quantified. This study was done by using the four dynamic models considered on six grids for $Re_\tau = 395$: see Table I. The simulations were performed on a single-core of an AMD 2.3 GHz Opteron Processor 6134 as a dedicated process using the torque queuing system. The time step, which was chosen on the basis of the finest grid resolution, was kept constant during all simulations. The central processing unit (CPU) time t (in s) for a single time step was calculated by dividing the computational time required to perform 500 time steps by 500. The values of t for the different grid resolutions are shown in Table I. It can be seen that the LDM requires the minimum amount of CPU time per time step followed by the DSM, NDM, and WBDM, respectively. The computational cost of the DSM are higher than the

TABLE I. CPU time (in s) for performing a numerical simulation over a single time step with the dynamic models considered for the specified grid resolutions.

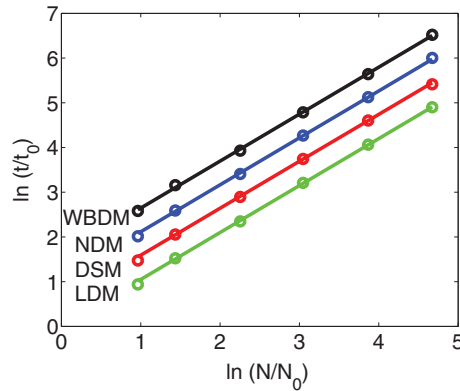| N	t^{DSM}	t^{LDM}	t^{NDM}	t^{WBDM}
$64 * 64 * 64$	6.48	6.26	6.76	7.23
$81 * 64 * 81$	11.60	11.23	12.04	12.85
$122 * 64 * 122$	26.88	25.63	27.21	27.83
$148 * 96 * 148$	62.83	60.65	64.28	65.51
$223 * 96 * 223$	148.35	142.50	151.70	154.08
$334 * 96 * 334$	333.64	329.18	364.99	371.33

FIG. 17. CPU time (in s) for performing a single time step of numerical simulation using the dynamic models considered for various grid resolutions. The data points are represented by circles and the fits are represented by solid lines. The DSM, NDM, and WBDM curves are shifted upwards by (0.5, 1.0, 1.5), respectively, to improve the visibility of the comparison between measured and modeled cost data.

LDM cost due to the need for performing averaging, clipping and also filtering of an additional term (the second term in H_{ij}: see Eq. (A2)) during the calculation of the dynamic constant. The increase of the computational time for the nonlinear models arises from the need to involve the nonlinear terms and to calculate additional dynamic constants. The NDM calculations are faster than the WBDM calculations because only a $2*2$ matrix needs to be inverted to calculate C_s^{NDM} and C_n^{NDM}, whereas a $3*3$ matrix inversion is needed for the calculation of the dynamic constants of the WBDM.

The following approach is used to quantify the computational time required for the use of the different models. An analysis of the Table I data provides support for the use of the relation

$$\frac{t}{t_0} = a \left(\frac{N}{N_0} \right)^b , \tag{23}$$

which relates the computational time t for performing a numerical simulation over a single time step to the number N of grid points applied. The introduction of the reference values $N_0 = 10^5$ and $t_0 = 2.45$ s here is helpful to simplify the model comparison ($t_0 = 2.45$ s implies $a = 1$ for the LDM). It turns out that the cost of all dynamic models considered are characterized by the same value $b = 1.05$. For each data point, the a values for the different dynamic models can be obtained by using Eq. (23). For each dynamic model, constant values of a can be calculated by taking the average over the a data obtained for each data point, where the first and last data points are not included. This leads to $a = (1.000, 1.043, 1.068, 1.101)$ for the LDM, DSM, NDM, and WBDM, respectively. The validity of using Eq. (23) in conjunction with these a values and $b = 1.05$ is confirmed in terms of Fig. 17, which shows a very good agreement between the measured cost data and the model (23). Note that the DSM, NDM, and WBDM curves are shifted upwards by (0.5, 1.0, 1.5), respectively, to improve the visibility of the comparison between measured and modeled cost data. The values $a = (1.000, 1.043, 1.068, 1.101)$ obtained for the LDM, DSM, NDM, and WBDM quantify the computational cost advantage of the LDM compared to the DSM, and the NDM compared to the WBDM. By using standard scalings for the number of grid points N required to compute a flow at a certain Reynolds number Re,[5] Eq. (23) can be used for representing t in dependence on Re.

VI. CONCLUSIONS

Many different dynamic LES methods were presented over the last two decades. Thus, there is the question of which dynamic method should be preferred. To have a basis for addressing this question, it was suggested here to characterize an optimal dynamic LES method by the properties P1-P5 given in Sec. I. A theoretical analysis showed recently that dynamic methods derived on the basis of stochastic analysis have the properties P1 and P2.[25] The goal of this paper was to use

a priori and *a posteriori* applications of these dynamic methods to provide evidence that the dynamic SGS stress models implied by stochastic analysis do also have the properties P3, P4, and P5 of an optimal dynamic SGS stress model. This goal was accomplished regarding the properties P3 and P4: the LDM and NDM allow negative model parameter values, and they enable computationally stable simulations without additional *ad hoc* assumptions. The latter conclusion was proven by simulations at different Reynolds numbers, $Re_\tau = (180, 395, 590, 950)$, on a variety of grids (see the grids involved in the cost analysis). The question of whether the LDM and NDM are also characterized by the property P5 (no other comparable dynamic method is either faster or more accurate) was addressed by comparisons with the non-stabilized and stabilized DSM, which is used in many applications of LES, and the WBDM, which represents an extension of the DSM. In difference to the realizable LDM and NDM, the DSM and WBDM do not represent realizable models because they are not derived as consequences of a realizable stochastic process.

A priori analyses of the non-stabilized DSM, WBDM, LDM, and NDM were used to study the suitability of formulations of dynamic models. An analysis of model errors showed very limited support for the basic assumption of the DSM approach that L_{ij}^d and H_{ij} are proportional to each other. On the other hand, the proportionality between L_{ij}^d and M_{ij} used in the LDM has a much higher level of support: the correlation value $r_{LM} = 0.5$ obtained away from the near-wall region is 2.5 times higher than the corresponding value $r_{LH} = 0.2$ obtained for the DSM. An analysis of the correlation coefficients R_L, R_τ, and R_P also showed that the LDM provides consistently significantly higher correlations than the DSM. Regarding the corresponding comparison of nonlinear dynamic models it was shown that the NDM always provides slightly higher correlation values than the WBDM, which represents an extension of Germano's dynamic concept.

A priori analyses of the non-stabilized DSM, WBDM, LDM, and NDM were also used to study the stability properties of dynamic models. Regarding the LDM it was shown that the stochastic modeling concept provides (without the use of any empirical clipping procedure) a natural clipping of dynamic constant values. The corresponding DSM feature is very different: the probability of very high positive or negative dynamic constant values can be by two orders of magnitude higher than the corresponding LDM probability for finding such dynamic constant values. The relatively high probability for very high negative dynamic constant values explains the DSM trend to become computationally unstable. The comparison of the NDM and WBDM shows that the structure of the PDFs of dynamic constants involved is very similar. Hence, the WBDM, which uses a dynamic model formulation in correspondence to the DSM, is computationally stable. Nevertheless, several observations support the view that there is no need for the introduction of the third dynamic constant involved in the WBDM. It appears that this third dynamic constant corresponds to the consideration of an additional noise source in dynamic calculations. Backscatter studies show that the DSM overpredicts the DNS backscatter in the near-wall region, which promotes the development of computational instabilities, whereas the LDM backscatter is below the DNS backscatter. The nonlinear NDM and WBDM models provide a significant improvement compared to the LDM, but such that their backscatter is below the DNS backscatter. Thus, the NDM and WBDM are found to be computationally stable.

A posteriori analyses of the stabilized DSM, WBDM, LDM, and NDM were used to study the accuracy of these dynamic methods. All the four dynamic models considered imply almost the same mean velocities and resolved Reynolds stresses. Differences are found with regard to instantaneous streamwise velocities. Due to the averaging and clipping involved, the DSM simulates turbulence structures that are smeared out and merged to large-scale structures, this means the small-scale structure of turbulence is not well represented. The LDM was shown to represent a better choice than the DSM. The LDM involves backscatter which enables an accurate representation of small-scale turbulence, and it is capable of correctly representing the typical streaky structures seen in the near-wall region of wall-bounded flows. Both the NDM and WBDM were found to provide predictions of instantaneous streamwise velocities that correspond to the LDM predictions.

A posteriori analyses of the stabilized DSM, WBDM, LDM, and NDM were also used to study the cost of these dynamic methods. The computational cost of all the dynamic models considered scale with the number of grid points N in the same way. The relative cost ratio of dynamic models, which is independent of N, is given by $a = (1.000, 1.043, 1.068, 1.101)$ for the LDM, DSM, NDM,

and WBDM, respectively. This result was obtained for N ranging from 0.3 to 10.7 $\times$ 10^6 grid points.

In summary, the comparisons reported here support the view that the LDM and NDM are based on a concept that is more appropriate than the concept used for obtaining the DSM and WBDM. The LDM and NDM account for backscatter, and they are computationally stable without any modification. The LDM and NDM represent the instantaneous small scale structure of turbulence very well. Compared to the DSM and WBDM, respectively, the LDM and NDM are computationally more efficient.

APPENDIX A: DYNAMIC SMAGORINSKY MODEL

The DSM applies $\tau_{ij}^d = -2C_s^{DSM}\Delta^2|\tilde{S}|\widetilde{S}_{ij}$ and $T_{ij}^d = -2C_s^{DSM}(\Delta^T)^2|\overline{\tilde{S}}|\overline{\tilde{S}}_{ij}$ for the deviatoric SGS and STS stresses, respectively. By using the latter expressions in Germano's identity $L_{ij}^d = T_{ij}^d - \overline{\tau_{ij}^d}$ we obtain

$$L_{ij}^d = -C_s^{DSM}H_{ij}, \tag{A1}$$

where the expression H_{ij} is given by

$$H_{ij} = 2\left(\Delta^T\right)^2|\overline{\tilde{S}}|\overline{\tilde{S}}_{ij} - 2\Delta^2\overline{|\tilde{S}|\widetilde{S}_{ij}}. \tag{A2}$$

Expression (A1) provides five conditions for C_s^{DSM}. The value of C_s^{DSM} is chosen such that it minimizes the squared error $E_{ij}^{DSM}E_{ji}^{DSM}$, where $E_{ij}^{DSM} = L_{ij}^d + C_s^{DSM}H_{ij}$. The optimal expression for C_s^{DSM} is given by

$$C_s^{DSM} = -\frac{L_{ij}^d H_{ij}}{H_{mn}H_{mn}}. \tag{A3}$$

The corresponding standardized quadratic error $e = |E|^2/|L^d|^2$ is given by $e_{DSM} = 1 - (r_{LH})^2$.

APPENDIX B: WANG-BERGSTROM DYNAMIC MODEL

The calculation of the dynamic constants in the WBDM follows Germano's approach, but it applies for the SGS and STS stresses nonlinear expressions,[15]

$$\tau_{ij}^d = -C_s^{WBDM}\beta_{ij} - C_w^{WBDM}\gamma_{ij} - C_n^{WBDM}\eta_{ij}, \tag{B1}$$

$$T_{ij}^d = -C_s^{WBDM}\alpha_{ij} - C_w^{WBDM}\lambda_{ij} - C_n^{WBDM}\zeta_{ij}. \tag{B2}$$

These models involve the expressions

$$\beta_{ij} = 2\Delta^2|\tilde{S}|\widetilde{S}_{ij}, \quad \gamma_{ij} = 4\Delta^2(\widetilde{S}_{ik}\widetilde{\Omega}_{kj} - \widetilde{\Omega}_{ik}\widetilde{S}_{kj}), \quad \eta_{ij} = 4\Delta^2(\widetilde{S}_{ik}\widetilde{S}_{kj} - \frac{1}{3}\widetilde{S}_{nk}\widetilde{S}_{nk}\delta_{ij}), \tag{B3}$$

$$\alpha_{ij} = 2\left(\Delta^T\right)^2|\overline{\tilde{S}}|\overline{\tilde{S}}_{ij}, \quad \lambda_{ij} = 4(\Delta^T)^2(\overline{\tilde{S}}_{ik}\overline{\tilde{\Omega}}_{kj} - \overline{\tilde{\Omega}}_{ik}\overline{\tilde{S}}_{kj}),$$

$$\zeta_{ij} = 4(\Delta^T)^2(\overline{\tilde{S}}_{ik}\overline{\tilde{S}}_{kj} - \frac{1}{3}\overline{\tilde{S}}_{nk}\overline{\tilde{S}}_{nk}\delta_{ij}). \tag{B4}$$

By using the latter expressions in Germano's identity we obtain

$$L_{ij}^d = -C_s^{WBDM} H_{ij} - C_w^{WBDM} W_{ij} - C_n^{WBDM} N_{ij}, \tag{B5}$$

where $H_{ij} = \alpha_{ij} - \overline{\beta}_{ij}$, $W_{ij} = \lambda_{ij} - \overline{\gamma}_{ij}$ and $N_{ij} = \zeta_{ij} - \overline{\eta}_{ij}$. The error related to specifications of model parameters is given by

$$E_{ij}^{WBDM} = L_{ij}^d + C_s^{WBDM} H_{ij} + C_w^{WBDM} W_{ij} + C_n^{WBDM} N_{ij}. \tag{B6}$$

The values of the dynamic constants are chosen such that they minimize the squared error $E_{ij}^{WBDM} E_{ji}^{WBDM}$. The optimal expression for the dynamic constants are the following ones:[15]

$$\begin{bmatrix} H_{ij}H_{ij} & H_{ij}W_{ij} & H_{ij}N_{ij} \\ W_{ij}H_{ij} & W_{ij}W_{ij} & W_{ij}N_{ij} \\ N_{ij}H_{ij} & N_{ij}W_{ij} & N_{ij}N_{ij} \end{bmatrix} \begin{bmatrix} C_s^{WBDM} \\ C_w^{WBDM} \\ C_n^{WBDM} \end{bmatrix} = - \begin{bmatrix} L_{ij}^d H_{ij} \\ L_{ij}^d W_{ij} \\ L_{ij}^d N_{ij} \end{bmatrix}. \tag{B7}$$

[1] C. Meneveau, "Statistics of turbulence subgrid-scale stresses: Necessary conditions and experimental tests," Phys. Fluids **6**(2), 815–833 (1994).

[2] P. J. Mason, "Large-eddy simulation: A critical review of the technique," Q. J. R. Meteorol. Soc. **120**(515), 1–26 (1994).

[3] M. Germano, "Fundamentals of large eddy simulation," in *Advanced Turbulent Flows Computations*, CISM Courses and Lectures Vol. 395, edited by E. Krause and R. Peyret (Springer, Berlin, 2000), pp. 81–130.

[4] U. Piomelli, "Large-eddy simulation: achievements and challenges," Prog. Aerosp. Sci. **35**(4), 335–362 (1999).

[5] S. B. Pope, *Turbulent Flows* (Cambridge University Press, Cambridge, 2000).

[6] C. Meneveau and J. Katz, "Scale-invariance and turbulence models for large-eddy simulation," Annu. Rev. Fluid Mech. **32**(1), 1–32 (2000).

[7] P. Sagaut, *Large Eddy Simulation for Incompressible Flows: An Introduction* (Springer-Verlag, Berlin, 2002).

[8] M. Lesieur, O. Metais, and P. Comte, *Large-Eddy Simulations of Turbulence* (Cambridge University Press, Cambridge, 2005).

[9] J. Smagorinsky, "General circulation experiments with the primitive equations," Mon. Weather Rev. **91**, 99–164 (1963).

[10] M. Germano, U. Piomelli, P. Moin, and W. H. Cabot, "A dynamic subgrid-scale eddy viscosity model," Phys. Fluids A **3**(7), 1760–1765 (1991).

[11] D. K. Lilly, "A proposed modification of the Germano subgrid-scale closure method," Phys. Fluids A **4**(3), 633–635 (1992).

[12] C. Meneveau, T. S. Lund, and W. H. Cabot, "A Lagrangian dynamic subgrid-scale model for turbulence," J. Fluid Mech. **319**, 353–385 (1996).

[13] T. S. Lund, S. Ghosal, and P. Moin, "Numerical experiments with highly variable eddy viscosity model," in *Engineering Applications of Large Eddy Simulations*, edited by S. A. Ragale and U. Piomelli, FED Vol. 162 (ASME, 1993), pp. 7–11.

[14] S. Ghosal, T. S. Lund, P. Moin, and K. Akselvoll, "A dynamic localization model for large-eddy simulation of turbulent flows," J. Fluid Mech. **286**, 229–255 (1995).

[15] B. C. Wang and D. J. Bergstrom, "A dynamic nonlinear subgrid-scale stress model," Phys. Fluids **17**, 035109 (2005).

[16] U. Piomelli and J. Liu, "Large-eddy simulation of rotating channel flows using a localized dynamic model," Phys. Fluids **7**, 839–848 (1995).

[17] S. Krajnovic and L. Davidson, "Large-eddy simulation of the flow around a bluff body," AIAA J. **40**(5), 927–936 (2002).

[18] S. Krajnovic and L. Davidson, "Large-eddy simulation of the flow around simplified car model," SAE Paper No. 2004-01-0227, Detroit, USA, 2004.

[19] A. E. Tejada-Martínez and K. E. Jansen, "A dynamic Smagorinsky model with dynamic determination of the filter width ratio," Phys. Fluids **16**, 2514–2528 (2004).

[20] L. Marstorp, G. Brethouwer, and A. V. Johansson, "A stochastic subgrid model with application to turbulent flow and scalar mixing," Phys. Fluids **19**(3), 035107 (2007).

[21] Y. Shi, Z. Xiao, and S. Chen, "Constrained subgrid-scale stress model for large eddy simulation," Phys. Fluids **20**, 011701 (2008).

[22] N. Park and K. Mahesh, "Reduction of the Germano-identity error in the dynamic Smagorinsky model," Phys. Fluids **21**, 065106 (2009).

[23] U. Piomelli, T. A. Zang, C. G. Speziale, and M. Y. Hussaini, "On the large-eddy simulation of transitional wall-bounded flows," Phys. Fluids A **2**, 257–265 (1990).

[24] W. W. Kim and S. Menon, "A new dynamic one-equation subgrid-scale model for large eddy simulations," AIAA Paper No. 1995-356, 1995.

[25] S. Heinz, "Realizability of dynamic subgrid-scale stress models via stochastic analysis," Monte Carlo Meth. Appl. **14**(4), 311–329 (2008).

[26] S. Heinz, "On Fokker–Planck equations for turbulent reacting flows. Part 2. Filter density function for large eddy simulation," Flow, Turbul. Combust. **70**(1), 153–181 (2003).

[27] S. Heinz, *Statistical Mechanics of Turbulent Flows*, 1st ed. (Springer-Verlag, Berlin, 2003).

[28] S. Heinz, "Comment on "A dynamic nonlinear subgrid-scale stress model"," Phys. Fluids **17**, 099101 (2005).

[29] S. Heinz, "Unified turbulence models for LES and RANS, FDF and PDF simulations," Theor. Comput. Fluid Dyn. **21**(2), 99–118 (2007).

[30] U. Schumann, "Realizability of Reynolds-stress turbulence models," Phys. Fluids **20**, 721–725 (1977).

[31] P. A. Durbin and C. G. Speziale, "Realizability of second-moment closure via stochastic analysis," J. Fluid Mech. **280**, 395–407 (1994).

[32] S. S. Girimaji, "A new perspective on realizability of turbulence models," J. Fluid Mech. **512**, 191–210 (2004).

[33] A. Andrén, "Evaluation of a turbulence closure scheme suitable for air-pollution applications," J. Appl. Meteor. **29**(3), 224–239 (1990).

[34] H. A. Wouters, T. W. J. Peeters, and D. Roekaerts, "On the existence of a generalized Langevin model representation for second-moment closures," Phys. Fluids **8**(7), 1702–1704 (1996).

[35] B. Merci, C. De Langhe, J. Vierendeels, and E. Dick, "A quasi-realizable cubic low-Reynolds eddy-viscosity turbulence model with a new dissipation rate equation," Flow, Turbul. Combust. **66**(2), 133–157 (2001).

[36] T. S. Park and H. J. Sung, "Development of a near-wall turbulence model and application to jet impingement heat transfer," Int. J. Heat Fluid Flow **22**(1), 10–18 (2001).

[37] J. R. Ristorcelli, J. L. Lumley, and R. Abid, "A rapid-pressure covariance representation consistent with the Taylor-Proudman theorem materially frame indifferent in the two-dimensional limit," J. Fluid Mech. **292**, 111–152 (2006).

[38] R. D. Moser, J. Kim, and N. N. Mansour, "Direct numerical simulation of turbulent channel flow up to $Re_\tau = 590$," Phys. Fluids **11**(4), 943–945 (1999).

[39] L. Y. M. Gicquel, P. Givi, F. A. Jaberi, and S. B. Pope, "Velocity filtered density function for large eddy simulation of turbulent flows," Phys. Fluids **14**, 1196–1213 (2002).

[40] M. R. H. Sheikhi, T. G. Drozda, P. Givi, and S. B. Pope, "Velocity-scalar filtered density function for large eddy simulation of turbulent flows," Phys. Fluids **15**(8), 2321–2337 (2003).

[41] P. Givi, "Filtered density function for subgrid scale modeling of turbulent combustion," AIAA J. **44**(1), 16–23 (2006).

[42] M. R. H. Sheikhi, P. Givi, and S. B. Pope, "Velocity-scalar filtered mass density function for large eddy simulation of turbulent reacting flows," Phys. Fluids **19**, 095106 (2007).

[43] M. R. H. Sheikhi, P. Givi, and S. B. Pope, "Frequency-velocity-scalar filtered mass density function for large eddy simulation of turbulent flows," Phys. Fluids **21**, 075102 (2009).

[44] S. Heinz, *Mathematical Modeling*, 1st ed. (Springer-Verlag, Heidelberg, 2011).

[45] D. K. Lilly, "The representation of small-scale turbulence in numerical simulation of experiments," in *Proceedings of the IBM Scientific Computing Symposium on Environmental Sciences*, edited by H. H. Goldstine (IBM, Yorktown Heights, NY, 1967), pp. 195–212.

[46] Y. Fabre and G. Balarac, "Development of a new dynamic procedure for the Clark model of the subgrid-scale scalar flux using the concept of optimal estimator," Phys. Fluids **23**(11), 115103 (2011).

[47] OPENFOAM, the open source CFD tool box, user guide, Version 1.6, 2009, see www.openfoam.org.

[48] R. I. Issa, "Solution of the implicitly discretised fluid flow equations by operator-splitting," J. Comput. Phys. **62**(1), 40–65 (1986).

[49] J. Gullbrand and F. K. Chow, "The effect of numerical errors and turbulence models in large-eddy simulations of channel flow, with and without explicit filtering," J. Fluid Mech. **495**, 323–341 (2003).

[50] J. Bredberg, S. H. Peng, and L. Davidson, "An improved k-ω turbulence model applied to recirculating flows," Int. J. Heat Fluid Flow **23**(6), 731–743 (2002).

[51] E. R. Van Driest, "On turbulent flow near a wall," J. Aeronaut. Sci. **23**(11), 1007–1011 (1956).

[52] U. Piomelli, W. H. Cabot, P. Moin, and S. Lee, "Subgrid-scale backscatter in turbulent and transitional flows," Phys. Fluids A **3**, 1766–1771 (1991).

[53] S. Hoyas and J. Jiménez, "Scaling of the velocity fluctuations in turbulent channels up to $Re_\tau = 2003$," Phys. Fluids **18**, 011702 (2006).

[54] W. Anderson, S. Basu, and C. Letchford, "Comparison of dynamic subgrid-scale models for simulations of neutrally buoyant shear-driven atmospheric boundary layer flows," Environ. Fluid Mech. **7**, 195–215 (2007).